SUPPLEMENTARY INFORMATION

Pulsed Laser Welding of Macroscopic 3D Graphene Materials

Wenjie Yu [a, b], Weiwei Zhao [a] & Xiaoqing Liu [a*]

1 Key Laboratory of Marine Materials and Related Technologies, Zhejiang Key Laboratory of Marine Materials and Protective Technologies, Ningbo Institute of Materials Technology and Engineering, Chinese Academy of Sciences, Ningbo, 315201, China

2 University of Chinese Academy of Sciences, Beijing, 100049, China

*Corresponding author:

Xiaoqing Liu, E-mail address: liuxq@nimte.ac.cn

Methods

Synthesis of PNE-a, PHE-a, and PPE-a

To synthesize PNE-a, PHE-a, and PPE-a, a benzoxazine intermediate was firstly prepared via the Mannich reaction with aniline (99.5%, 62-53-3), paraformaldehyde (96.0%, 30525-89-4) and pyrogallol (97.0%, 87-66-1) as raw materials. Specifically, 500 mL ethyl acetate (99.9%, 141-78-6) as the solvent, 1.07 mol aniline, and 1.16 mol paraformaldehyde were added into a 1000 mL round-bottom flask equipped with a reflux condenser; the mixture was stirred at 60 ^{o}C for 1.5 h. Then the reaction temperature was raised to 75 ^{o}C followed by introducing 1.50 mol paraformaldehyde and 0.53 mol pyrogallol. After another 4 h of reaction, the precipitation was obtained by direct filtration. Finally, the white product was washed using ethanol and dried in a 50 °C vacuum oven to give the benzoxazine intermediate (yield: 75%).

For the synthesis of PNE-a, 0.15 mol triethylamine (99.5%, 121-44-8) as an acid acceptor, 0.1 mol benzoxazine intermediate, and 400 mL chloroform (99.0%, 67-66-3) as solvent were introduced into a round-bottom flask with a magnetic stirrer. Then, a solution prepared with 100 ml chloroform and 0.15 mol nonyl chloride (96.0%, 764-85-2) was added dropwise into the mixture under stirring in an ice water bath. After 24 h of reaction, the mixture was washed with deionized water for 5 times. Finally, the PNE-a was obtained after removing the solvent using a rotary evaporator. PHE-a and PPE-a were synthesized following the similar steps, in which the nonyl chloride was replaced by heptyl chloride (2528-61-2, 99%) and pentanoyl chloride (638-29-9, 98%), respectively (yield: 88%).

Laser transformation of adhesive precursors into LIG structures

A commercial CO_2 laser cutter system (Universal VLS3.50, USA) with a 10.6 μm laser wavelength, a pulse duration of ~14 ms, a pulse frequency of ~5 kHz, a focal length of 50.8 mm, and a focus spot diameter of 127 μm was used for laser-induced transforming. The laser scanning speed was set to 7.5 inch/s, and the z-axis distance of the surface of the samples from the focal plane was fixed at 2.6 mm. For the characterization of LIG structures, 0.20 g PHE-a as precursor was first injected on a Si supporting substrate

placed on a 90 °C heating plate. The thickness of PHE-a was controlled to be ~75 μm using a hand roller. The precursor was then cooled down to room temperature and subjected to twice laser irradiation to produce the LIG solder structures, in which the laser power was 7.4 and 4.4 W in sequence.

Ni-solder, Fe-solder, and N-solder were fabricated following a similar procedure for characterization, in which the precursor was modified by mixing 0.20 g PHE-a with 0.04 g nickel (II) acetylacetonate (95%, 3264-82-2), 0.04 g iron (III) acetylacetonate (98%, 14024-18-1), and 0.08g melamine (99.0%, 108-78-1), respectively.

Precursor infiltration and pyrolysis process

The LIG-1 was produced by infiltrating the additional PHE-a into the original LIG solder structure and lasing the same area. Specifically, PHE-a was over-injected onto the original LIG solder structure placed on a 90 °C heating plate. The liquid PHE-a spontaneously entered the inner pores of LIG under the interfacial tensions. After 5 min of infiltration, the sample was removed from the heating plate and cooled down to the RT. The excessive precursor was then scraped off the surface of LIG using a 90 °C hot blade. Finally, the sample was lased using the same laser parameters for fabricating the original LIG solder. The LIG-2 and LIG-3 were produced by repeating the above procedures.

Preparation of base graphene materials

The various free-standing porous graphene films served as base materials for welding were prepared according to the literature. For example, the base graphene films with a strength of 2.73 MPa and a conductivity of 6600 S/m were produced via a bottom-up approach we previously developed.[1] Briefly, a poly(Ph-ddm) resin was first laser irradiated to fabricate a high-quality porous graphene layer at laser power of 13.1 W, laser scanning rate of 7.5 inch/s, laser spot size of 134 μm, and image density of 7. Then, the formed graphene layer was separated from the polymer substrate by rapid quenching in liquid nitrogen to offer a free-standing porous graphene film with a thickness of ~40 μm. In addition, the other base graphene materials including the films

decorated with different elements and the large-size films for 3D construction were readily produced as described in our previous study.[2]

Butt joint welding of porous graphene films

Before welding, one end of each base material was placed on a Si supporting substrate. The adhesive precursor at 90 °C was then over-injected between them to butt them together. The distance between the two base structures was controlled depending on the experiments. The liquid precursor physically turned into a gelled semisolid state upon naturally cooling. Afterwards, the precursor thickness was tailored to be ~75 μm by a heated handle roller and a 90 °C hot blade was used to scrape the excessive precursor off the surface of base structures. The precursor thickness was controlled so that the resultant solder matched the base material in thickness. Eventually, the precursor was transformed into LIG solder by twice pulsed laser irradiating to realize the welding of graphene materials, in which the laser power was 7.4 and 4.4 W in sequence. The overlap scanning was performed to ensure the high quality of the welded junction.

Lap welding of porous graphene films

A base graphene film with a lateral size of 15 mm × 15 mm as the underlying structure was placed on a hot plate, the temperature of which was optimized to ~50 °C. 0.02 g adhesive precursor was then covered on the film's top surface. The relatively low operating temperature was set to decrease the flowability of the precursor. Subsequently, another graphene film of the same lateral size was laid as the upper graphene layer. Finally, a 1.0 kg weight was stacked on the upper layer to bond them together. Removing the spilled precursor by a hot blade and then exposing the laminated graphene structure to twice laser irradiation, the final Janus structure was obtained. The applied laser power was 7.4 and 4.4 W in sequence.

Of note, all laser welding experiments were conducted under ambient conditions and used the same laser parameters: 7.5 inch/s scanning rate, 134 μm laser spot size, 1000 pulse per inch, and 7 image density. After laser irradiation, all products were immersed

in acetone for 10 min to remove the residual precursor and then dried in a 50 °C vacuum oven for 30 min before testing

Characterization methods

^{1}H and ^{13}C NMR spectra of synthesized compounds were recorded at 25 °C on a Bruker AVIII400 NMR spectrometer (Karlsruhe, Germany). Chemical shifts (δ) were reported with TMS serving as a reference of all nuclides. Rheological analysis was performed on a Discovery Hybrid Rheometer (TA, USA). DSC analysis of the adhesive precursor was performed on a Mettler-Toledo MET DSC (METTLER TOLEDO, Switzerland) at a cooling rate of 10 °C/min under N_2 atmosphere. The contact angle was measured using a video optical contact angle meter, OCA20 (Dataphysics, Germany) at room temperature. XPS data were collected using an X-ray photoelectron spectroscopy (Axis Ultra DLD, Kratos), and the binding energies were referenced to C1s peak (284.5 eV). Raman analysis was performed with a confocal Raman spectrometer (Renishaw inVia Reflex, Renishaw) using 532 nm laser excitation and 8 mW laser power. Raman mapping data were recorded in a continuous line scan mode with a step size of 4.0 μm. XRD patterns were measured on an X-ray diffraction (D8 Advance, Bruker) with Cu Kα radiation (λ = 1.5405 Å). SEM coupled with EDS analysis was conducted on a large cavity scanning electron microscope, EVO18 (ZEISS, Germany) at 20 kV. TEM images were captured using a Talos F200X instrument (ThemoFisher) at an operating voltage of 200 kV. The thickness of LIG solders was determined by a thickness tester (CHY-CA, China) with an accuracy of ± 1 μm. The mass of samples was determined by a balance (ME 104, Mettler Toledo), and the density was calculated as mass divided by volume. The conductivity value was translated from the electric resistance which was evaluated by a DC power supply (MCH-K3010DN). The tensile test was conducted on a universal testing machine (Zwick/Roell Z1.0, Germany) with a stretching rate of 2 mm/min.

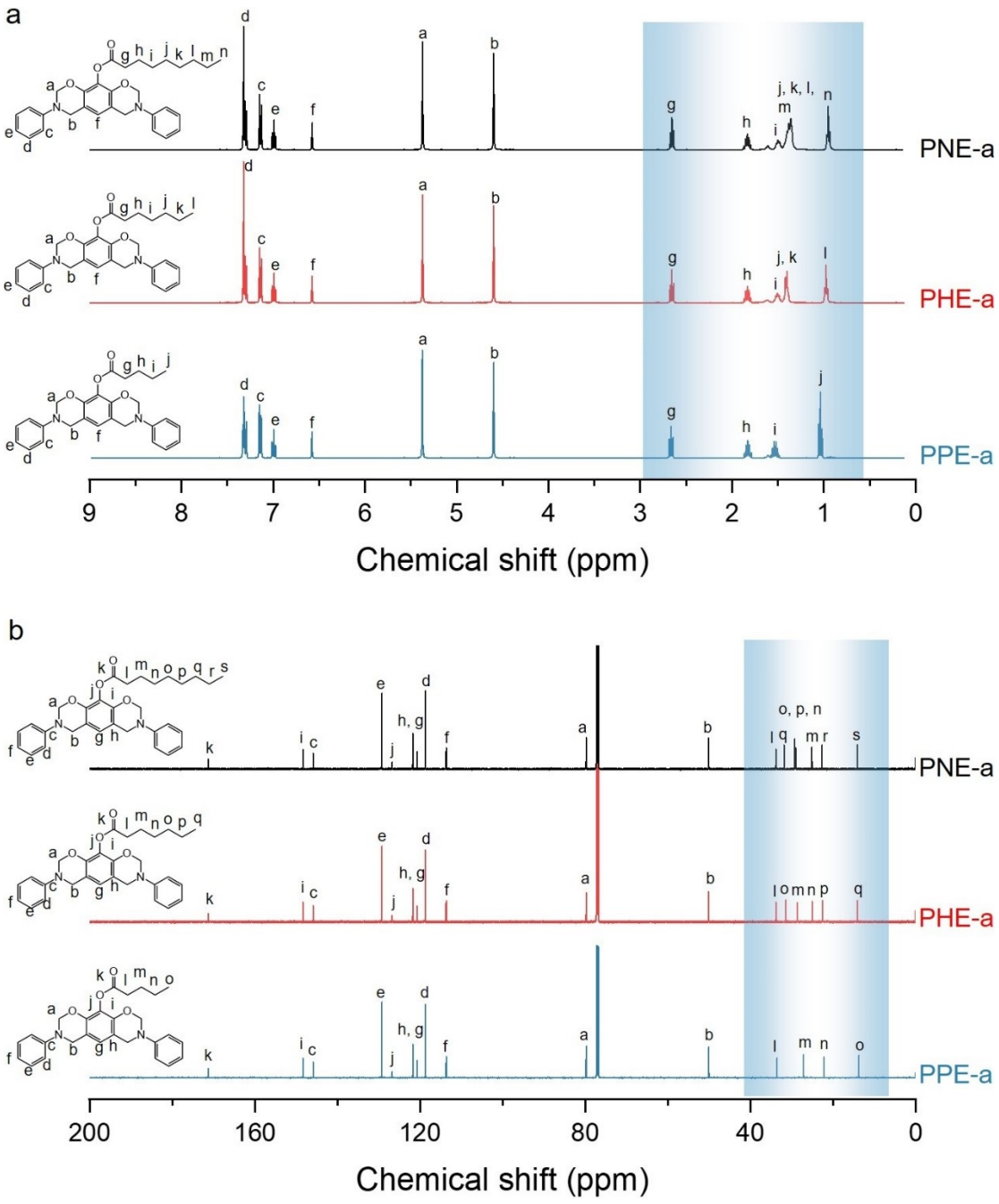

Figure S1: Chemical structure characterization of synthesized PNE-a, PHE-a, and PPE-a. a) ^{1}H NMR spectra ($CDCl_3$, 400 MHz). (b) ^{13}C NMR spectra ($CDCl_3$, 101 MHz). PPE-a: ^{1}H NMR (400 MHz, Chloroform-d) δ = 7.34 – 7.28 (m, 4H), 7.18 – 7.10 (m, 4H), 7.00 (td, J = 7.3, 1.1 Hz, 2H), 6.58 (s, 1H), 5.38 (s, 4H), 4.60 (s, 4H), 2.67 (t, J = 7.5 Hz, 2H), 1.83 (p, J = 7.5 Hz, 2H), 1.59 – 1.48 (m, 2H), 1.04 (t, J = 7.4 Hz, 3H). ^{13}C NMR (151 MHz, Chloroform-d) δ = 171.21, 148.34, 145.88, 129.25, 126.76, 121.77, 120.71, 118.69, 113.69, 79.79, 50.07, 33.57, 27.10, 22.19, 13.75. PHE-a: ^{1}H NMR (400 MHz, Chloroform-d) δ = 7.36 – 7.26 (m, 4H), 7.18 – 7.10 (m, 4H), 7.04 –

6.95 (m, 2H), 6.58 (s, 1H), 5.37 (s, 4H), 4.60 (s, 4H), 2.66 (t, J = 7.5 Hz, 2H), 1.83 (p, J = 7.5 Hz, 2H), 1.55 – 1.47 (m, 2H), 1.44 – 1.34 (m, 4H), 1.02 – 0.94 (m, 3H). ^{13}C NMR (151 MHz, Chloroform-d) δ = 171.22, 148.35, 145.88, 129.26, 126.76, 121.77, 120.71, 118.70, 113.69, 79.78, 50.09, 33.87, 31.47, 28.68, 25.05, 22.58, 14.06. PNE-a: ^{1}H NMR (400 MHz, Chloroform-d) δ = 7.35 – 7.26 (m, 4H), 7.18 – 7.10 (m, 4H), 7.04 – 6.95 (m, 2H), 6.58 (s, 1H), 5.37 (s, 4H), 4.60 (s, 4H), 2.66 (t, J = 7.5 Hz, 2H), 1.83 (p, J = 7.5 Hz, 2H), 1.50 (m, J = 7.6 Hz, 2H), 1.45 – 1.31 (m, 8H), 0.99 – 0.90 (m, 3H). ^{13}C NMR (151 MHz, Chloroform-d) δ = 171.23, 148.35, 145.89, 129.26, 126.76, 121.77, 120.71, 118.69, 113.69, 79.78, 50.09, 33.87, 31.85, 29.26, 29.04, 25.11, 22.68, 14.12.

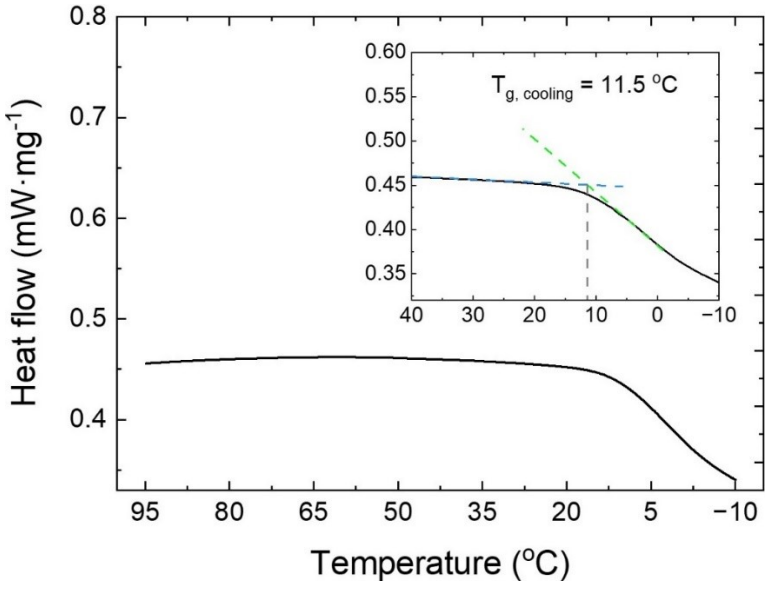

Figure S2: DSC curves of PHE-a. As shown, the glass transition appears when the temperature dropped below 11.5℃.

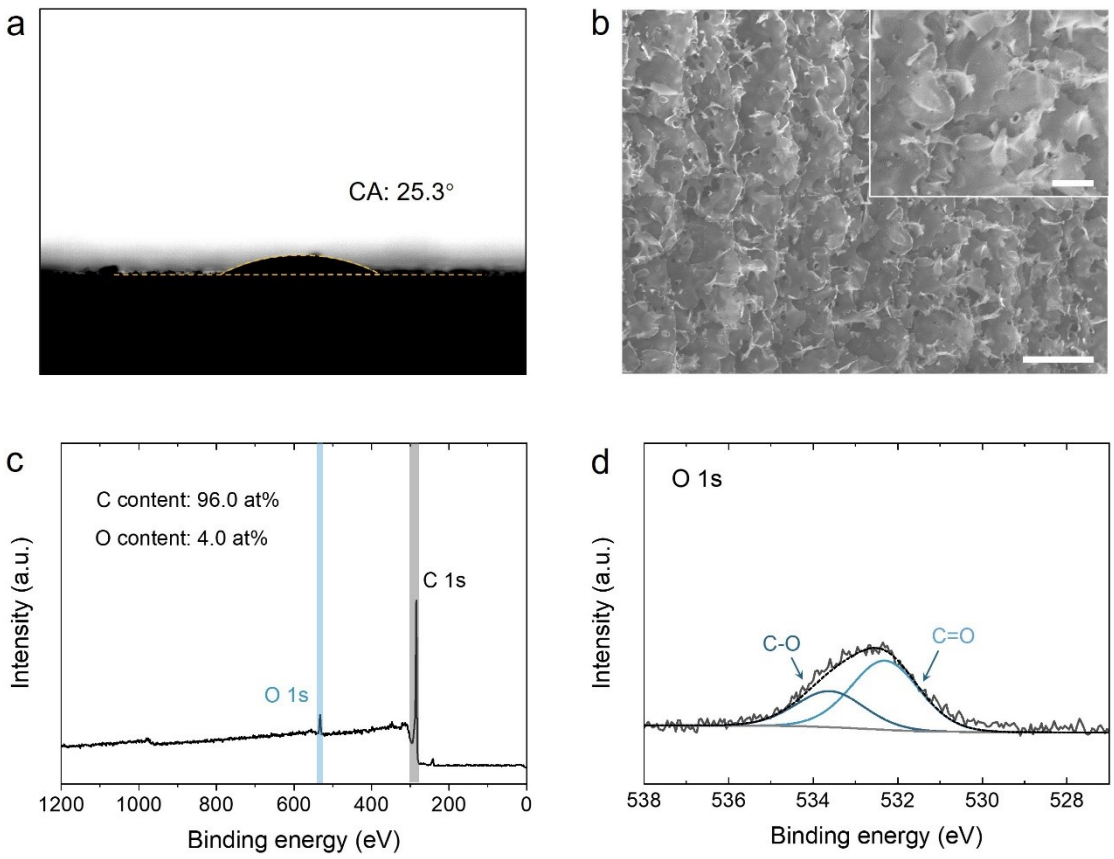

Figure S3: a) Contact angle between PHE-a and a base graphene film. For measurement, the molten precursor of ~ 50 µL was first dropped on the surface of the graphene film placed on a 90 °C heating plate. After 10 s of standing, the entire material system was transferred to the test bench at room temperature for characterizing. b) Surface morphology of the base graphene film; the scale bar is 30 µm. Inset is an enlarged version; the scale bar is 10 µm. c) XPS spectra of the base graphene film, showing a dominant C 1s peak and extremely low oxygen content of ~4.0 at%. d) The XPS O 1s spectrum was deconvoluted into two peaks that were assigned to C-O (~533.5 eV) and C=O (~532.3 eV).

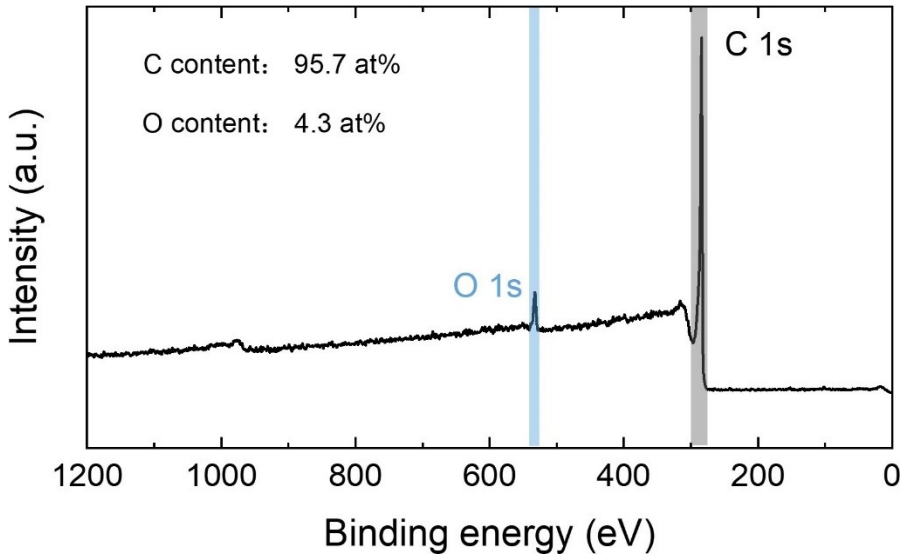

Figure S4: XPS spectrum of LIG solder.

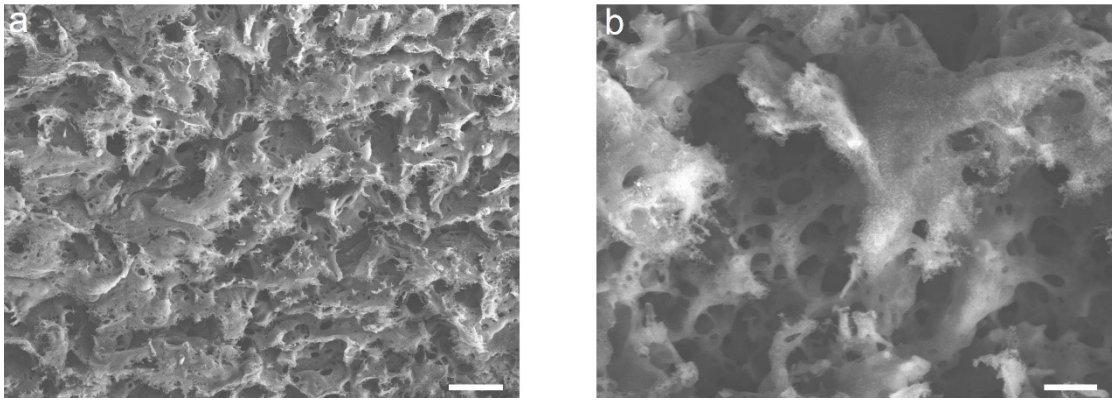

Figure S5: Porous morphology of LIG solder at a) low magnification and b) high magnification; the scale bars are 50 μm and 10 μm, respectively.

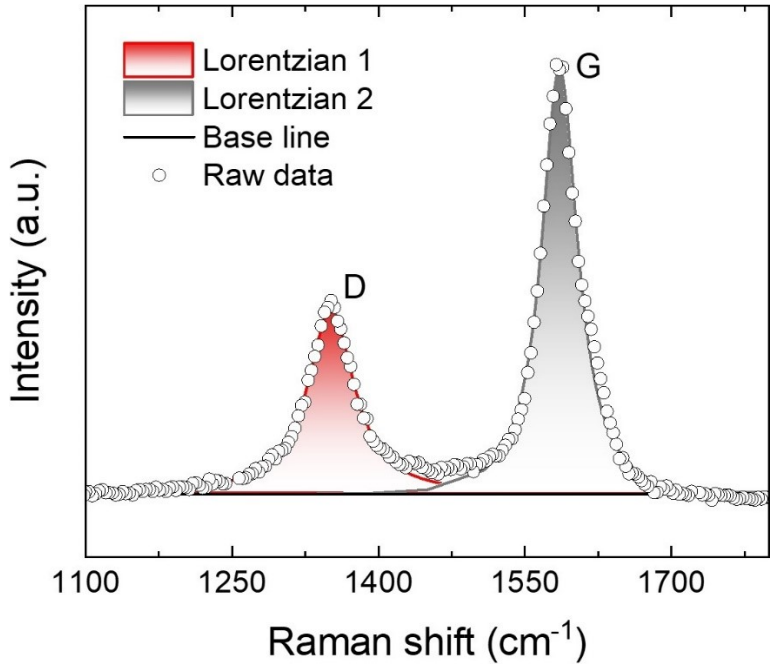

Figure S6: Curve fitting for the Raman D and G peak of the solder. The D peak at 1351 cm^{-1} results from defects or bent sp^2-carbon bonds. The G peak centered at 1585 cm^{-1} possesses an FWHM of 44 cm^{-1}, suggesting a high graphitization level of LIG solder.[3]

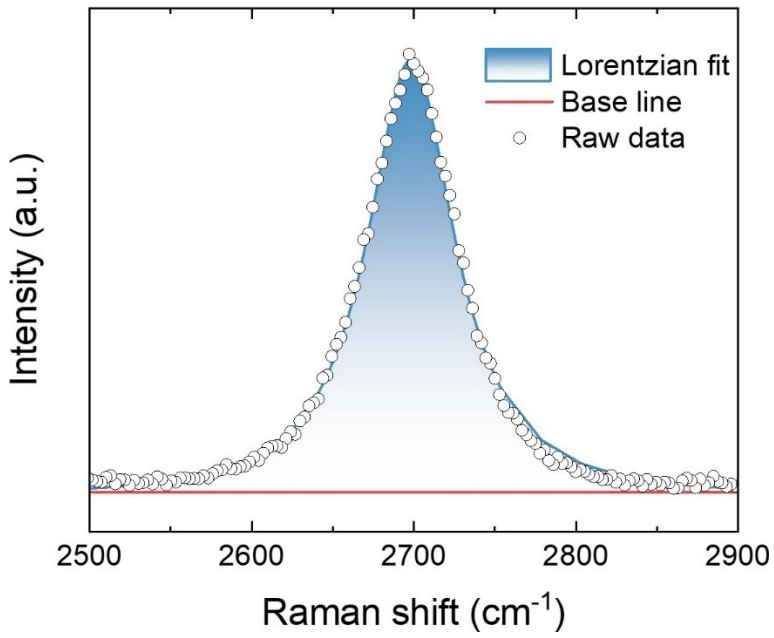

Figure S7: Curve fitting for the Raman 2D peak of the solder. The 2D peak at 2698 cm^{-1} possesses a single Lorentzian shape with an FWHM of ~ 64 cm^{-1}.

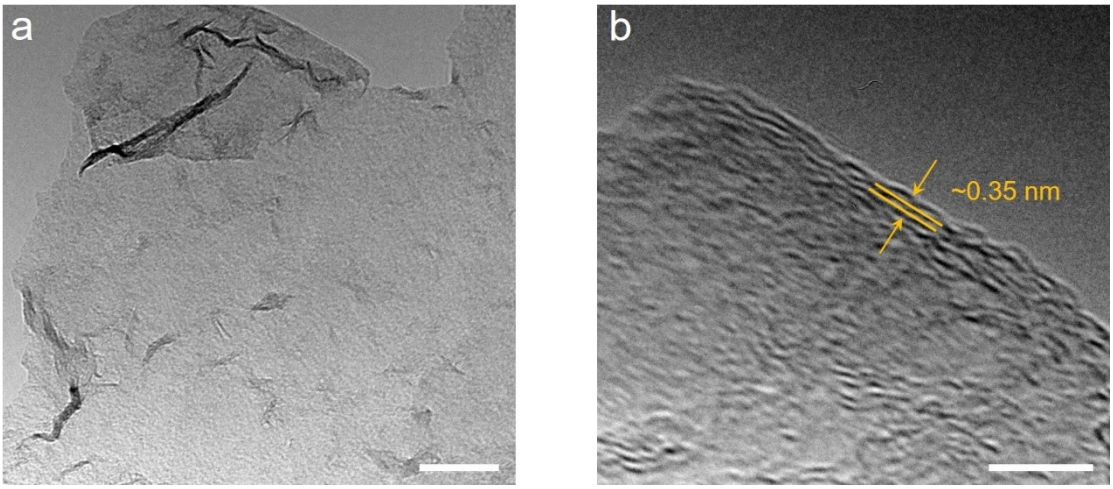

Figure S8: a) TEM image and b) HRTEM image of the edge of the solder flake; the scale bars are 50 nm and 5 nm.

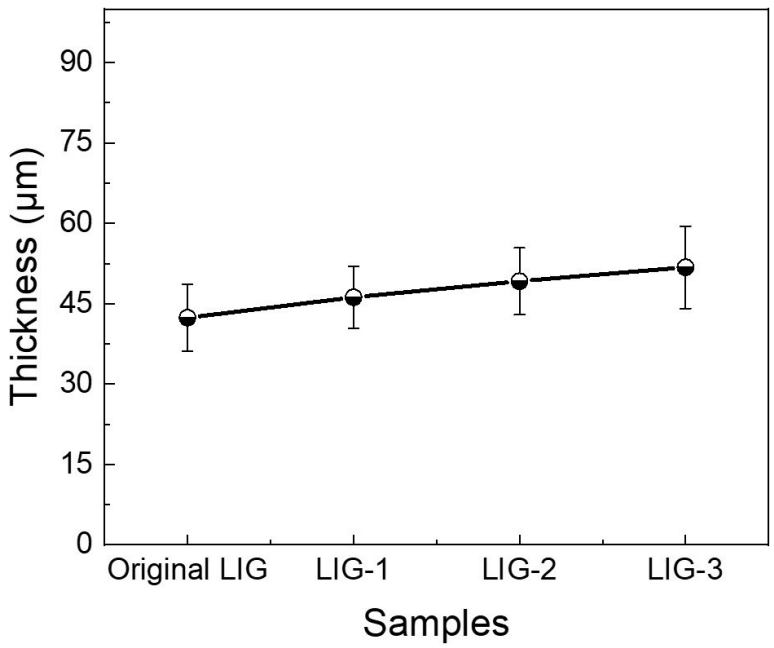

Figure S9: Thickness of original LIG, LIG-1, LIG-2, and LIG-3. The original LIG solder was produced from the adhesive precursor of ~75 μm.

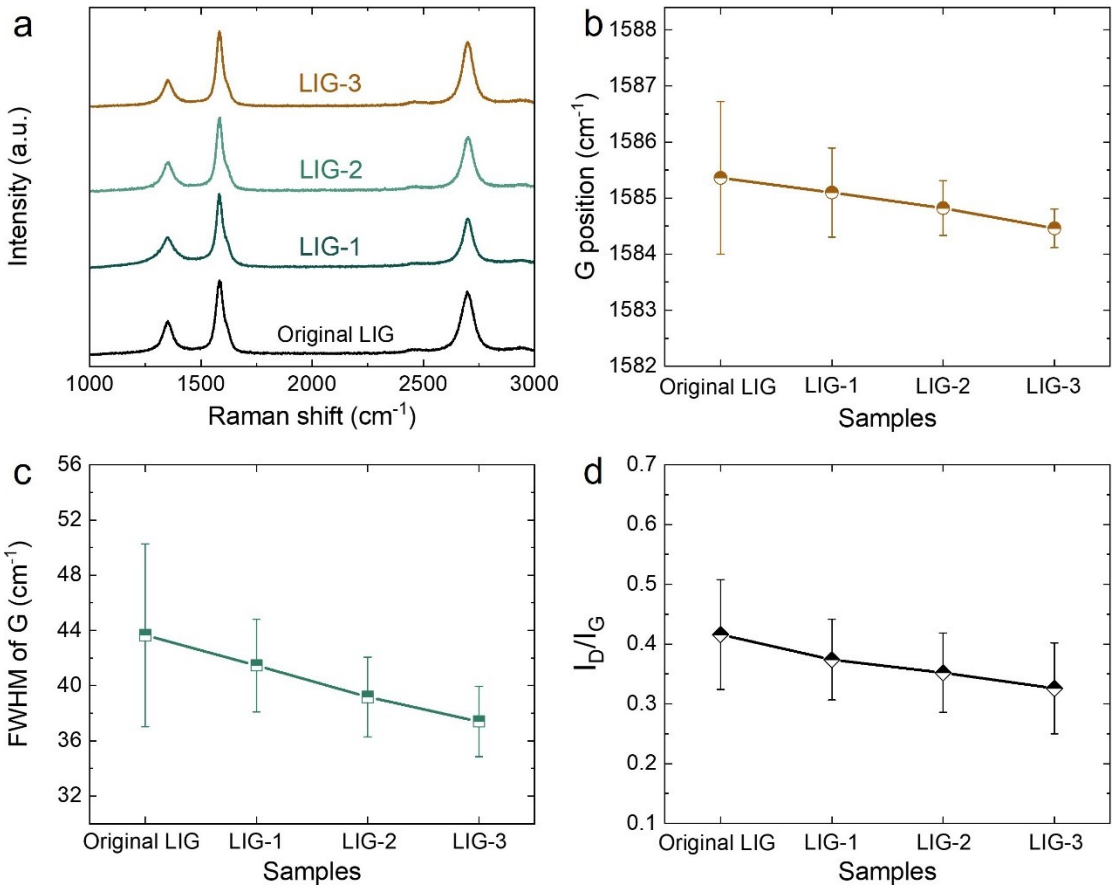

Figure S10: a) Representative Raman spectra of LIG solders that underwent different precursor infiltration and pyrolysis times. Statistical analysis of b) G position, c) FWHM of G peak, and d) I_D/I_G of samples. The standard deviation was calculated based on five repeated experiments.

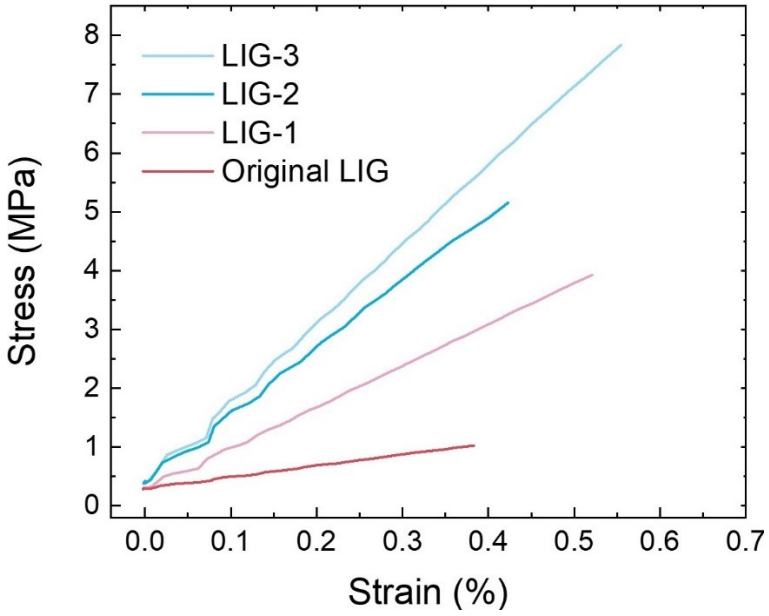

Figure S11: Representative tensile stress-strain curves of the different LIG solder.

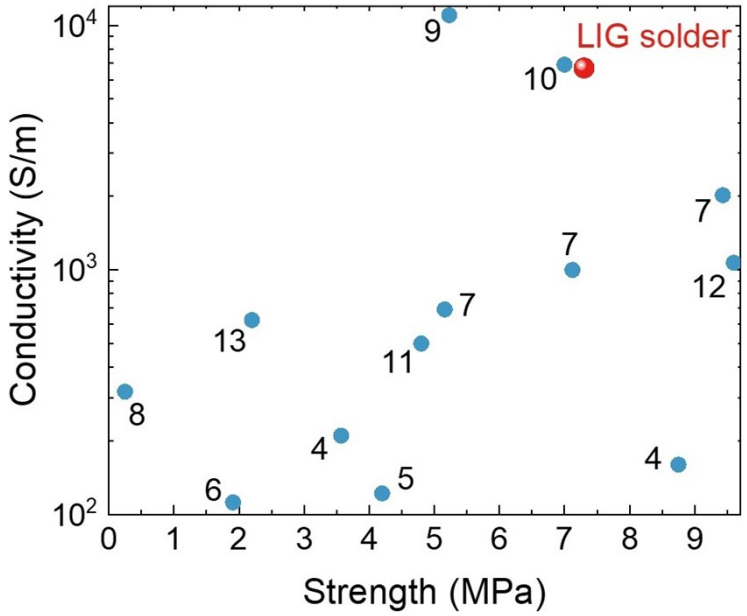

Figure S12: Comparison of the LIG solder with 3D graphene materials previously reported in terms of conductivity and strength.[4-13]

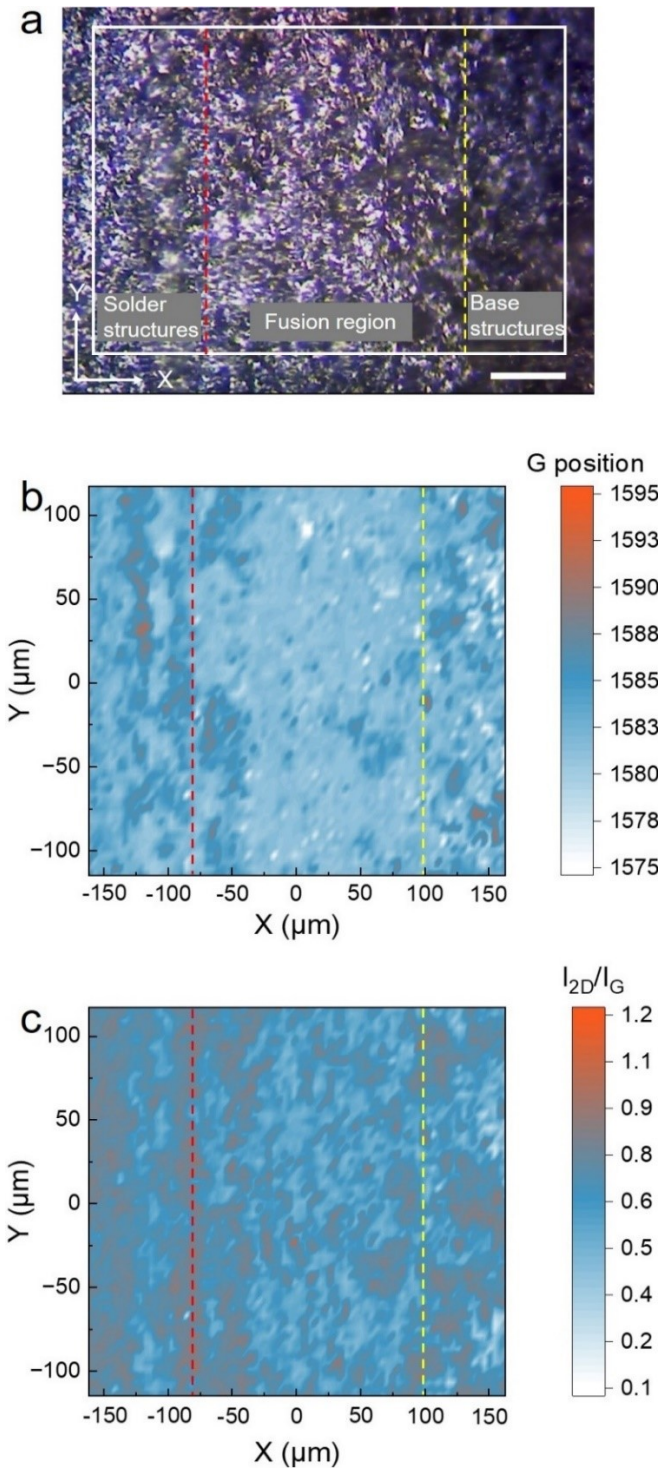

Figure S13: a) Optical image of the junction part of solder and base graphene structures; the scale bar is 50 μm. Corresponding Raman b) G position and c) I_{2D}/I_G mapping images. The red dashed lines are used to distinguish the solder structures and fusion structures, and the yellow dashed lines are used to distinguish the base structures and fusion structures.

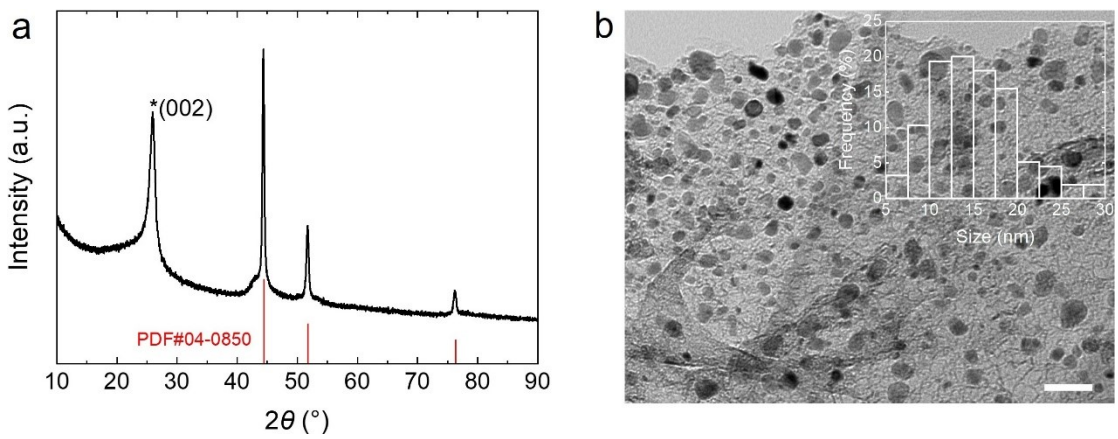

Figure S14: a) XRD pattern of the Ni-solder. The PDF reference card is Ni, 04-0850. The peak at ~26° (star) is attributed to the multi-layer graphene structure. b) TEM image shows that Ni nanoparticles evenly distribute on the solder flake with roughly a normal distribution size; the scale bar is 50 nm. Inset is the particle size distribution calculated based on the statistical analysis of the projected area diameter of Ni nanoparticles.

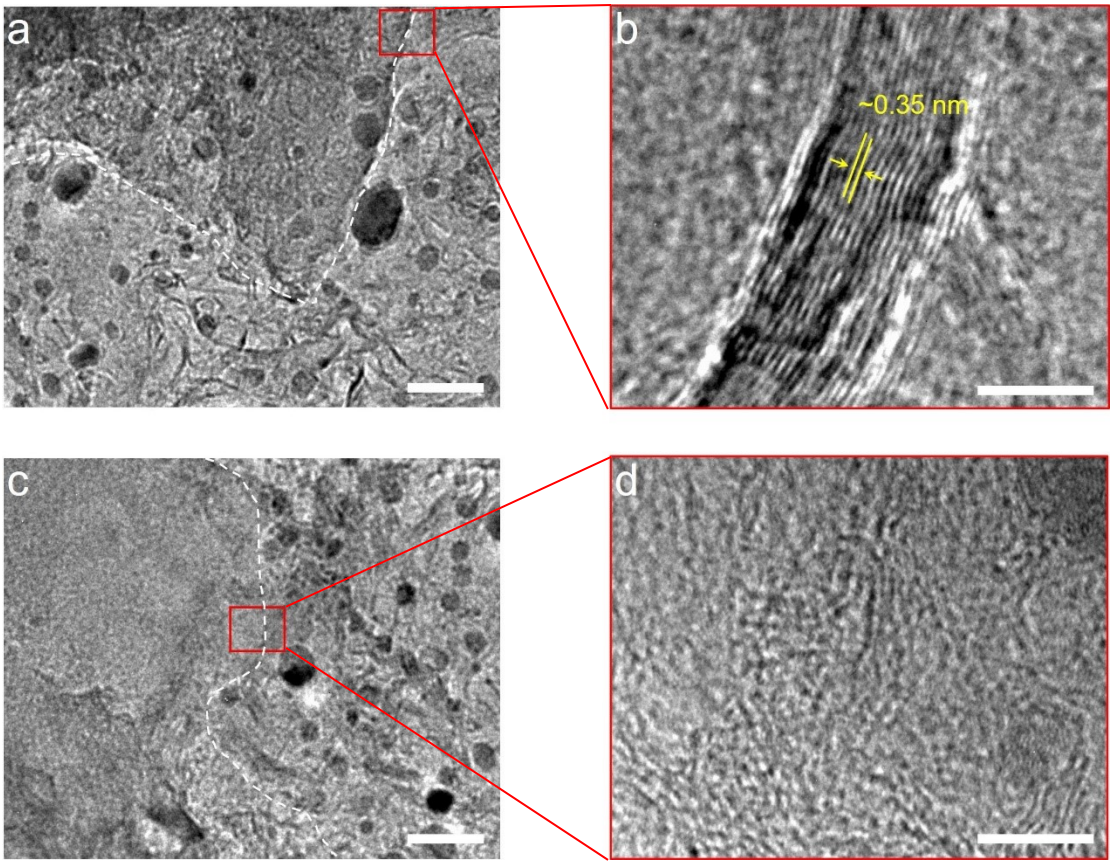

Figure S15: a) A TEM image of the layer-to-layer welding structure; the scale bar is 30 nm. The multi-layer stacking structural feature is further detailed by b) an HRTEM image; the scale bar is 5 nm. c) TEM image and d) HRTEM image of the integrated welding structure show a roughly continuous graphene flake with Ni-solder and base structures; the scale bars are 30 nm and 5 nm, respectively. The white dashed lines are used to roughly outline base graphene structures. Presumably, the formation mechanism of the integrated welding structure was conceptually similar to the repair of graphene holes and edge defects by carbon sources at high temperatures, which have been well demonstrated in the research relevant to graphene nanomanufacturing.[14, 15]

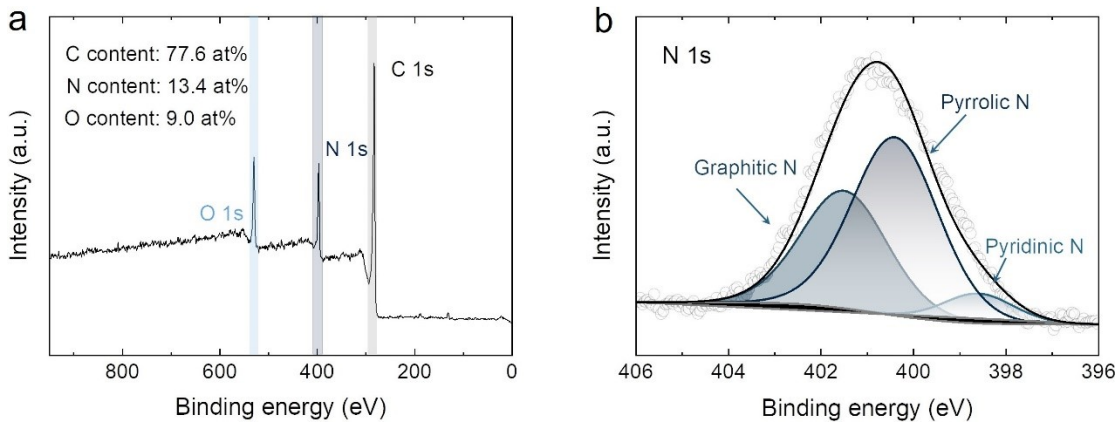

Figure S16: a) XPS spectrum of N-solder. The N-doping level is calculated to be 13.4 at%. b) High-resolution XPS N 1s spectra of N-solder. The N 1s peak can be deconvoluted into three sub-peaks located at ~398.5 eV, 400.4 eV, and 401.5 eV, which may be respectively attributed to pyridinic N, pyrrolic N, and graphitic N.[16]

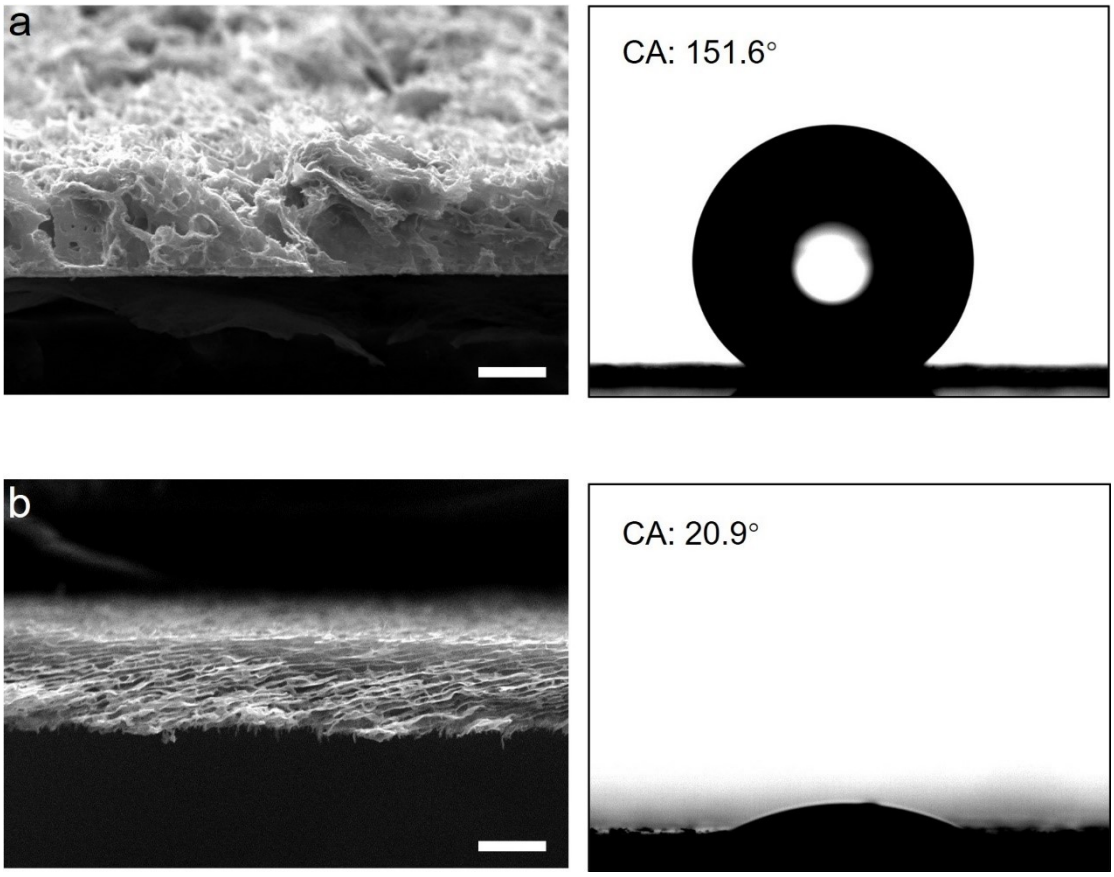

Figure S17: The characterization of two base graphene films used to fabricate the Janus structure. a) SEM image of the upper film (right) and its water contact angle (left); the scale bar is 30 μm. b) SEM image of the underlying one (right) and its water contact angle (left); the scale bar is 30 μm.

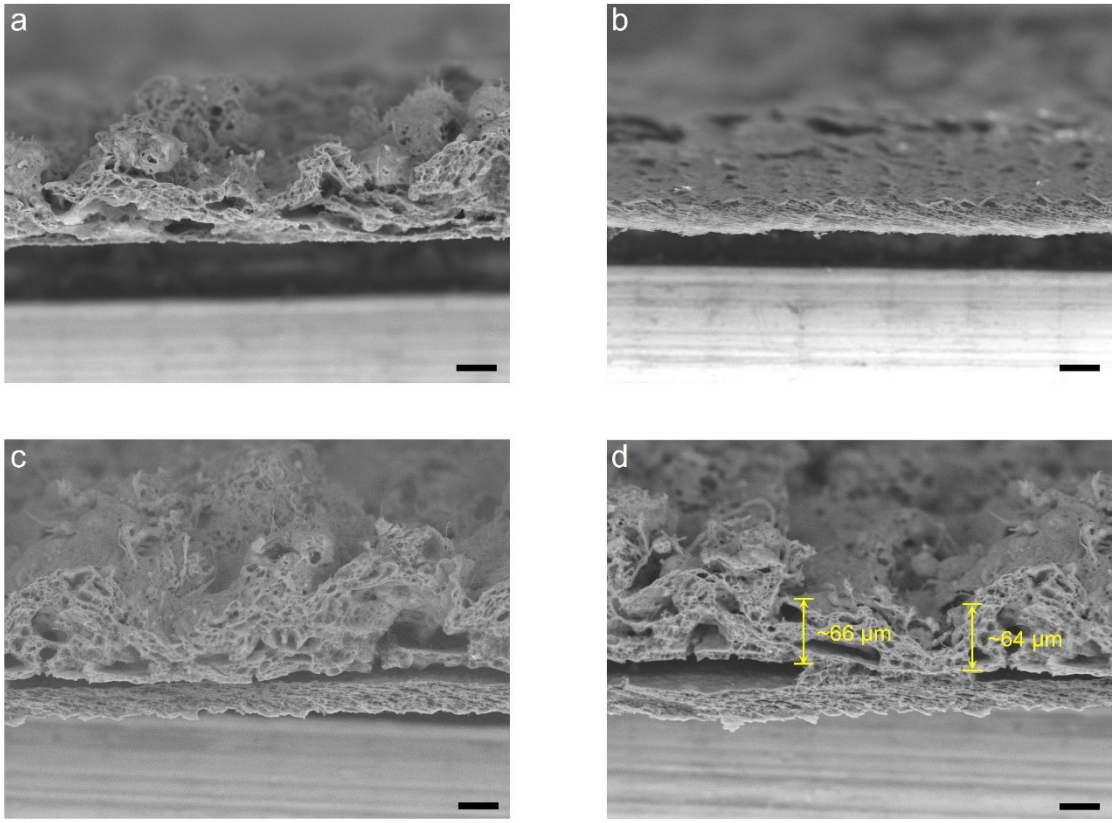

Figure S18: The investigation of the critical thickness of the upper layer for lap welding. a) a graphene film with a non-uniform thickness and b) a graphene film with a uniform thickness of ~40 µm are respectively employed as the upper layer and underlying one for the welding. c) The SEM image shows that lap welding is completely unfeasible if the thickness of the upper layer is too large. d) The SEM image shows that the critical thickness of the upper layer structure is roughly 65 µm. The scale bars are 40 µm.

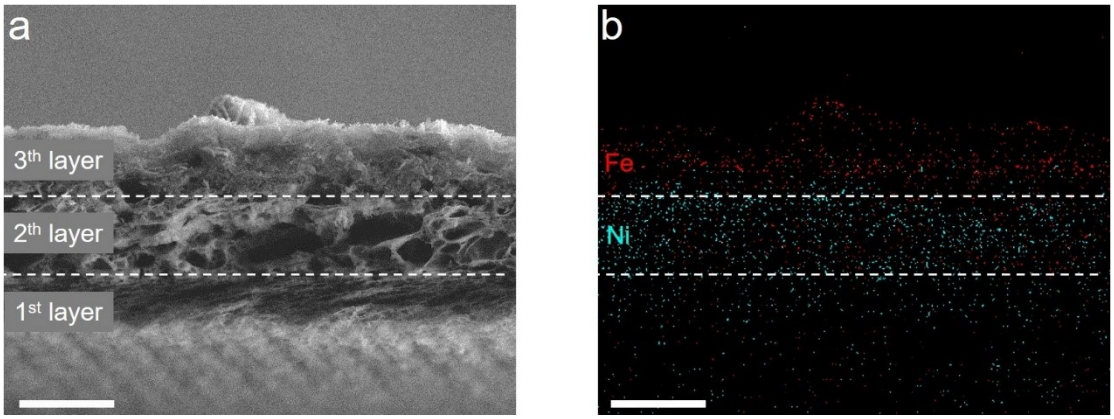

Figure S19: a) SEM image of a three-layer graphene film fabricated by forming Ni-solder and Fe-solder on a base film in sequence; the scale bar is 20 μm. b) EDS elemental mapping derived from a); the scale bar is 20 μm.

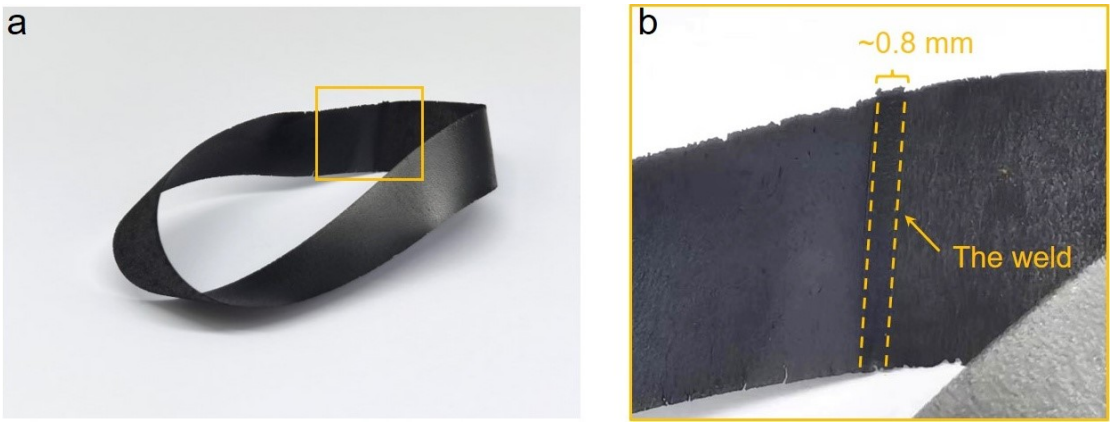

Figure S20: A graphene Möbius strip fabricated from a free-standing graphene film with the dimension of 160 mm × 14 mm × 40 μm. a) Digital image of as-made Möbius strip. b) A magnification of the weld.

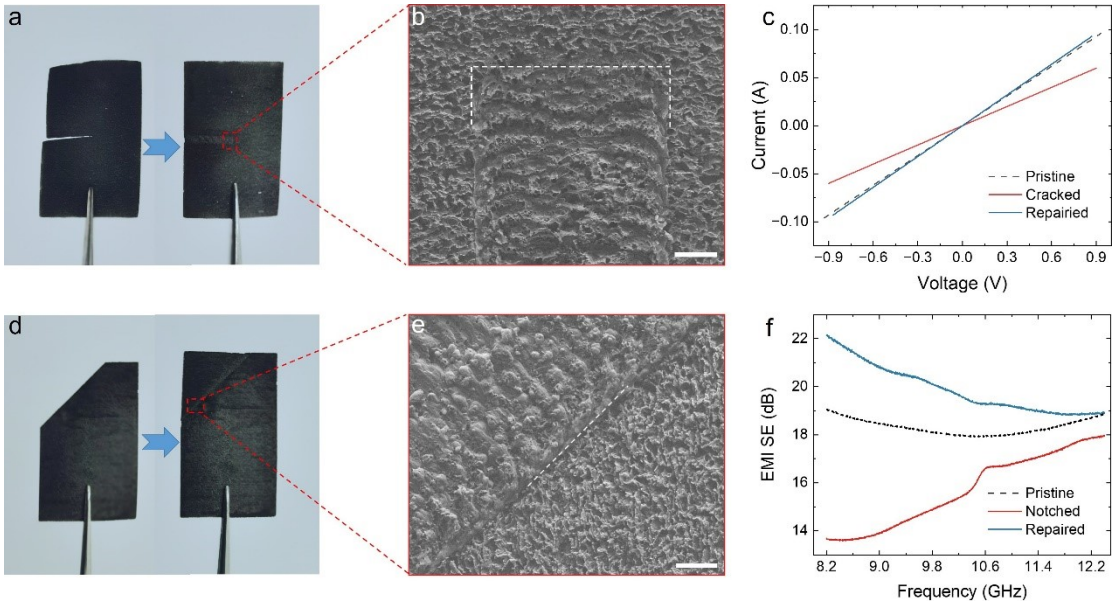

Figure S21: a) A cracked graphene film repaired via PLW. b) SEM image of the repaired part; the scale bar is 200 μm. c) I-V curves of the pristine, cracked, and repaired graphene films. d) A notched graphene film repaired via PLW. e) SEM image of the junction part of base structures and solder structures; the scale bar is 200 μm. f) EMI SE of the pristine, the notched, and the repaired graphene films at the frequency of 8.2~12.8 GHz.

Supplementary References

1. W. Yu, Y. Peng, L. Cao, W. Zhao and X. Liu, *Carbon*, 2021, **183**, 600-611.
2. W. Yu, W. Zhao, S. Wang, Q. Chen and X. Liu, *Adv. Mater.*, 2023, **35**, 2209545.
3. C. J. X. Zang, S. Ingersoll, Huashan Li, J. J. Adams, Z. Lu, N. Ferralis, J. C. Grossman, *Sci. Adv.*, 2020, **6**, 5231.
4. Y. Wang, Y. Wang, P. Zhang, F. Liu and S. Luo, *Small*, 2018, **14**, 1802350.
5. Y. Gao, Y. Zhai, G. Wang, F. Liu, H. Duan, X. Ding and S. Luo, *Adv. Sci.*, 2022, **9**, 2200362.
6. Z. Xiong, C. Liao, W. Han and X. Wang, *Adv. Mater.*, 2015, **27**, 4469-4475.
7. D. Lai, X. Chen, G. Wang, X. Xu and Y. Wang, *J. Mater. Chem. C*, 2020, **8**, 8904-8916.
8. H. Bi, Z. Liu, F. Xu, Y. Tang, T. Lin and F. Huang, *J. Mater. Chem. A*, 2016, **4**, 11762-11767.
9. M. Zhang, W. Wang, L. Tan, M. Eriksson, M. Wu, H. Ma, H. Wang, L. Qu and J. Yuan, *Energy Storage Mater.*, 2021, **35**, 327-333.
10. L. Zhang, Y. Chen, Q. Liu, W. Deng, Y. Yue and F. Meng, *J. Mater. Sci. Technol.*, 2022, **111**, 57-65.
11. Z. Song, W. Li, Y. Bao, H. Kong, S. Gan, W. Wang, Z. Liu, Y. Ma, D. Han and L. Niu, *ACS Appl. Nano Mater.*, 2020, **3**, 1731-1740.
12. Y. Zhang, M.-K. Xu, Z. Wang, T. Zhao, L.-X. Liu, H.-B. Zhang and Z.-Z. Yu, *Nano Research*, 2022, **15**, 4916-4924.
13. M. Huang, C. Wang, L. Quan, T. H.-Y. Nguyen, H. Zhang, Y. Jiang, G. Byun and R. S. Ruoff, *Matter*, 2020, **3**, 487-497.
14. H. Huang, X. Ming, Y. Wang, F. Guo, Y. Liu, Z. Xu, L. Peng and C. Gao, *Carbon*, 2021, **180**, 197-203.
15. Y. Chen, Y. Wang, S. Zhu, K. Fu, X. Han, Y. Wang, B. Zhao, T. Li, B. Liu, Y. Li, J. Dai, H. Xie, T. Li, J. W. Connell, Y. Lin and L. Hu, *Mater. Today*, 2019, **24**, 26-32.
16. F. Zhang, E. Alhajji, Y. Lei, N. Kurra and H. N. Alshareef, *Adv. Energy Mater.*, 2018, **8**, 1800353.